East European Journal of Physics. **2.** 138-146 (2026)
DOI:10.26565/2312-4334-2026-2-13 ISSN 2312-4334

IMPACT OF DIRECT AND PULSED ELECTRODEPOSITION MODE ON THE ELECTROCHEMICAL, STRUCTURAL, AND MORPHOLOGICAL PROPERTIES OF Ni-Fe NANOSTRUCTURES COATINGS

Houssem Eddine El Yamine Sakhraoui[1,2], H. Ayadi[3], N. Maouche[2], D. Belfennache[4], R. Yekhlef[4], Mohamed A. Ali[5], Hamad M. Adress Hasan[6], Hanan F. Emrayed[6], Haneebal Saeid Khatab[7], Ghada M. Salem[8]
[1]Département de Génie des Procédés, Faculté de Technologie, Université de Ferhat Abbas Sétif-1, Sétif, 19000, Algeria
[2]Laboratoire d'Electrochimie et Matériaux (LEM), Université de Ferhat Abbas Sétif-1, Sétif, 19000, Algeria
[3]Université 20 Août 1955 de Skikda, Skikda, Algeria
[4]Research Center in Industrial Technologies CRTI, P.O. Box 64, Cheraga, 16014 Algiers, Algeria
[5]School of Biotechnology, Badr University in Cairo (BUC), Badr City 11829, Cairo, Egypt
[6]Chemistry Department, Faculty of Science, Omar Al-Mukhtar University, Libya
[7]Chemistry Department, Faculty of Education, Al-Marj, University of Benghazi, Libya
[8]Libyan Authority for Scientific Research, Tripoli, Libya
**Correspondence Author e-mail: belfennachedjamel@gmail.com*

Received February 12, 2026; revised April 28, 2026; accepted May 5, 2026

Nickel-iron (Ni-Fe) nanostructured alloys are attracting increasing interest due to their remarkable electrochemical, magnetic, and mechanical properties, making them particularly attractive for applications in electrocatalysis, energy storage, sensors, and functional coatings. This study presents a comparative analysis of the electrochemical, structural, and morphological characteristics of nickel-iron (Ni-Fe) nanostructures synthesized in sulfate electrolytes on indium tin oxide (ITO) substrates through various electrodeposition methods. The fabricated nanostructures were characterized using cyclic voltammetry, chronoamperometric measurements (potentiostatic steps), atomic force microscopy (AFM), and X-ray diffraction (XRD). The electro-crystallization process was evaluated using the Scharifker-Hills model, revealing that nucleation mechanisms differed based on applied potentials. XRD analysis confirmed the polycrystalline nature of the Ni-Fe nanostructures, with a preferred <111> crystallographic orientation and a face-centered cubic (fcc) structure observed in both deposition modes. The crystallite sizes were determined as 9.77 nm under pulsed conditions and 14.63 nm for the direct method. AFM surface analyses further demonstrated that the choice of electrodeposition method significantly influences the morphological features of the resulting deposits.

Keywords: *Ni-Fe nanostructures; Electrodeposition method; Coatings; ITO substrate*
PACS: 61.46.Df, 61.82.Rx

1. INTRODUCTION

The earliest documented paint-based coatings originated in Europe and Australia around 20,000 years ago [1]. During this period, formulations included iron oxide, chalk, or charcoal, applied using fingertips or brushes crafted by splitting soft twigs [1]. In contrast, ancient Egyptian and Greek civilizations developed more sophisticated coating technologies, including early polymeric-based paints and coatings [2]. Historians often classify nanotechnology as a reinvented field, noting that early efforts to create nanoscale coatings emerged in ancient Egypt and were later refined in China [2]. In recent years, nanomaterials and nanotechnology-based coatings have become a focal point of scientific research, both for fundamental understanding and technological innovation. This surge is driven by their diverse applications and expanding utility in response to growing social and industrial demands [3].

Among these, nickel (Ni) and nickel-based coatings have emerged as critical materials in various industries, gaining significant attention for their diverse applications [4,5]. These include uses in electronics—such as memory and storage devices for computers—enhancing substrate hardness and wear resistance, and in components like transducers, transformers, and protective chokes [6,7]. Additionally, nickel coatings are vital for corrosion protection, energy storage systems, and solar thermal applications [8-10]. The surge in nickel and nickel-coating research stems from the versatility of their preparation methods. For instance, composite coatings incorporating nanoparticles such as Al_2O_3 [11], ZrO_2 [12], Si_3N_4 [13], In_2O_3 [14], SiC [15] enhance matrix properties by dispersing these particles. Alternatively, crystallite refinement through additives [16] and alloying with elements such as Tungsten (W) [17], Chrome (Cr) [18], Molybdenum (Mo) [19], and Cobalt (Co) [20] further expand their applicability. Crucially, the synthesis technique employed directly impacts the resulting coating properties.

Several synthesis techniques are used to develop coatings [21-24]; however, electrochemistry [25] is among the most advantageous methods for producing nanocoatings. Among the numerous synthesis approaches reported in the

---

Cite as: H.E. El Yamine Sakhraoui, H. Ayadi, N. Maouche, D. Belfennache, R. Yekhlef, M.A. Ali, H.M.A. Hasan, H.F. Emrayed, H.S. Khatab, G.M. Salem, East Eur. J. Phys. 2, 138 (2026), https://doi.org/10.26565/2312-4334-2026-2-13

literature, electrochemical synthesis stands out for its high adaptability and its ability to precisely control the structural, morphological, and functional properties of the resulting materials [26,27].

The variety of its processes provides a good synthesis of diversified nano-coatings in terms of both quantity and quality [28,29] in organic [30,31] and inorganic [32] fields. With a good manipulation of the sequence parameters, it is possible to design the desired properties of nano-coatings, such as their thickness and morphology [26]. Based on the low costs and reduced amount of waste materials, the electrochemical process has given rise to increasing interest in alloy electrodeposition, particularly in modern electronic devices. The present study investigates the effect of electrodeposition mode on the, morphology, and functional properties of Ni–Fe alloy coatings, with particular emphasis on the process–structure– morphology property relationship

2. MATERIALS AND METHODS

2.1. Techniques of characterization

X-ray diffraction (XRD) patterns of the powder were obtained using an analytical X'pert-PRO diffractometer equipped with Cu Kα radiation.

Electrochemical measurements were conducted in a conventional three-electrode cell. Potential values were referenced to a saturated calomel electrode (SCE), positioned close to the cathodic steel surface to minimize ohmic potential drops in the electrolyte. A platinum grid served as the auxiliary electrode. Indium tin oxide (ITO)-coated conducting glass substrates were employed as working electrodes, featuring an exposed area of 1 cm² and a sheet resistance of 10–20 Ω/cm². Prior to use, the substrates were cleaned via ultrasonic degreasing in acetone and ethanol for 10 minutes, followed by thorough rinsing with distilled water.

2.2. Chemicals

The sources of nickel and iron available for reduction in the solution are the $NiSO_4.6H_2O$ and $FeSO_4.7H_2O$ (Sigma-Aldrich). The aim of adding boric acid H_3BO_3 (Sigma-Aldrich) in the electrolyte is to avoid the pH variation near the electrode and to inhibit the formation of hydroxide species. The Sodium sulfate $Na_2SO_4.6H_2O$ was used as supporting electrolyte and used to maintain the overall quality of the electrodeposits. The bath composition and operating conditions are gathered in Table 1.

Table 1. Electrolyte composition and operating parameters

Bath composition	$NiSO_4.6H_2O$ (0.05 M) $FeSO_4.6H_2O$ (0.05 M) $Na_2SO_4.6H_2O$ (0.1 M) 0.05 M H_3BO_4 (0.05 M) pH 3.7-.5
Operating parameter	Temperature (°C) 23-25
Cathode	ITO substrates
Anode	Pt grid
Reference	Saturated calomel electrode (ECS)

2.3 Preparation of synthetic solution of Ni-Fe alloy

Nickel-iron (Ni-Fe) alloy nanostructures were synthesized through the reduction of Fe^{2+} and Ni^{2+} ions in an aqueous solution, using 0.1 M sodium sulfate ($Na_2SO_4·6H_2O$) as the supporting electrolyte. Nickel sulfate ($NiSO_4·6H_2O$, 30 mmol) and iron sulfate ($FeSO_4·6H_2O$, 10 mmol) were dissolved uniformly in 200 mL of distilled water. The solution was stirred magnetically for 10 minutes at room temperature, after which 0.05 M boric acid (H_3BO_3) was added to adjust the pH to a range of 3.7–5.0. To investigate the electrochemical kinetics and growth mechanisms of Ni, Fe, and Ni-Fe alloy electrodeposition, cyclic voltammetry (CV) and chronoamperometry (CA) were employed. The nucleation behavior of the deposits was further analyzed using the Scharifker-Hills model to interpret transient current responses during deposition [33].

3. RESULTS AND DISCUSSION

3.1. Cyclic voltammetry of Nickel, Iron and Ni-Fe

To determine the potential range over which nickel and iron deposition occur, cyclic voltammetry was carried out. The electrolyte solution contains 0.05 M of $FeSO_4$, H_3BO_3, and 0.1 M Na_2SO_4.

Fig. 1 shows cyclic voltammograms of the cathodic part for Ni electrodeposited onto an ITO substrate. The beginning of the current decrease was detected at -1100 mV/SCE, which indicates the over potential deposition process onto the ITO surfaces. The presence of cross-overs in the positive and negative scans is a typical sign of the formation of a new phase, involving nucleation followed by a diffusion-limited growth process [34]. It is also noticed that the hydrogen evolution reaction (HER) might occur simultaneously with nickel deposition.

The electrodeposition of nickel was first proposed by the adsorption of a nickel complex, then a reaction of charge transfer in two stages according to the following mechanism [35]:

$$Ni^{2+} + OH^{-} \rightarrow Ni(OH)^{+} \quad (1)$$

$$Ni(OH)^{+} + e^{-} \rightarrow Ni(OH)_{ads} \quad (2)$$

$$Ni(OH)_{ads} + e^{-} \rightarrow Ni + (OH)^{-} \quad (3)$$

The adsorbed monovalent nickel intermediate may also undergo reduction as:

$$Ni^{2+} + 2e^{-} + Ni(OH)_{ads} \rightarrow Ni + Ni(OH)_{ads} \quad (4)$$

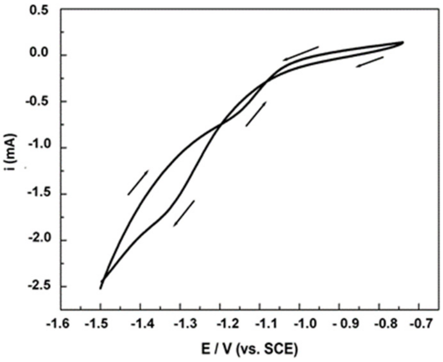

Figure 1. Cyclic voltammogram of Ni deposited on Pt electrode in aqueous solution containing 0.05 M of $NiSO_4$, H_3BO_3 and 0.1 M Na_2SO_4 at a scan rate of 100 mV/s

Fig. 2 shows the cyclic voltammogram for Fe electrodeposition. It reveals two reduction reactions for Fe^{2+} ions: one yields Fe+ ions, and the other yields metallic Fe. The scan was performed between -0.6 and -1.6 V/ESC at a scan rate of 100 $mV{\cdot}s^{-1}$. The current decrease was detected at -0.7 and -1.00 V/ SCE, which is characteristic of the over potential deposition of the Fe^{2+} reduction process to the adsorbed Fe^{+} then to the metallic iron Fe [36].

$$Fe^{2+} + e^{-} \rightarrow Fe^{+}_{ads} \quad (5)$$

$$Fe^{+}_{ads} + e^{-} \rightarrow Fe \quad (6)$$

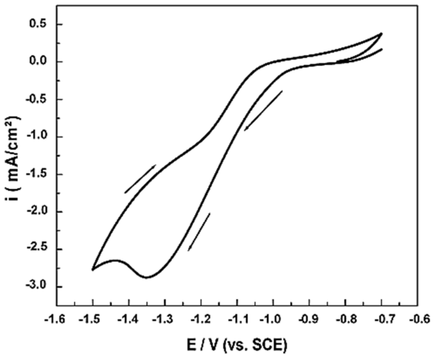

Figure 2. Cyclic voltammogram of Fe deposited in aqueous solution containing 0.05 M of $FeSO_4$, H_3BO_3, and 0.1 M of Na_2SO_4 at a scan rate of 100 mV/s

Fig. 3 represents the cyclic voltammogram of Ni-Fe. In the positive scan, the current decreased at 1000 mV, corresponding to the reduction of Ni and Fe. In the reverse scan, a dissolution pic of the previously formed species (Ni and Fe) was observed around -625 mV, and their oxidation at 355 mV.

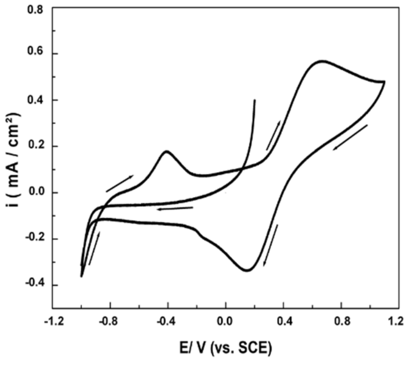

Figure 3. Cyclic voltammogram of Ni-Fe deposited in aqueous solution containing 0.05 M of $FeSO_4$, H_3BO_3, $NiSO_4$, and 0.1 M Na_2SO_4 at a scan rate of 100 mV/s

3.1.1 Ni-Fe electrodeposition mechanism

Dahms was to be the first to try to explain the inhibition function of the observed codeposition alloy Ni-Fe behavior [37]. The pH value on the cathodic surface is supposed to be high because of the following secondary reaction:

$$2H^+ + 2e^- \to H_2 \tag{7}$$

It was proposed that codeposition is due to the concurrent reaction of hydrogen release, which becomes very awkward for nickel deposition. Because of this condition, the pH of the surface could increase, thus enabling the formation of metal hydroxides according to the reaction:

$$M^{2+} + 2OH^- \to M(OH)_2, \tag{8}$$

$$Ni^{2+} + 2OH^- \to Ni(OH)_{2\,aq}, \tag{9}$$

$$Fe^{2+} + 2OH^- \to Fe(OH)_{2\,aq}. \tag{10}$$

Where M represents: Ni and Fe.

Consequently, it was noted that the nickel reduction was inhibited, which may be due to the preferential adsorption of ferrous hydroxides on the cathodic surface. These ferrous hydroxides block the available sites at the electrode surface. Giuliani and Lazzari [38] supposed that during the codeposition of Ni-Fe alloy, the reduction of the H^+ and Ni^{2+} ions occurs in the first step, causing an increase in the pH of the cathode surface, then the formation of $Ni(OH)^+$ and $Fe(OH)^+$. Gangasingh and Talbot [39] have proposed a very similar mechanism as that of Dahms and Croll.[37] for the Ni-Fe codeposition. The difference was that Ni^{2+} and Fe^{2+} were taken to form aqueous hydroxides $Ni(OH)_{2\,(aq)}$ and $Fe(OH)_{2\,(aq)}$ instead of solid hydroxides of the reactions according to the following homogeneous reactions:

3.1.2 Hydrogen evolution reaction (HER)

On the cathodic part in the sulphate medium, hydrogen evolution reaction (HER) intervenes which devised into several stages. The first stage, called stage of *Volmer* corresponds to the formation of an adsorbed MH_{ads} type intermediary, by adsorption of protons on the surface of metal. The second stage is an electrochemical desorption after the adsorption of a new H^+ (stage of *Heyrovsky*) and/or a chemical desorption after the recombination of two adsorbed intermediaries (stage of *Tafel*), these three stages are given below:

$$M + H^+ + e^- \to MH_{ads}\ \textit{Volmer}, \tag{11}$$

$$MH_{ads} + H^+ + e^- \to H_2 + M\ \textit{Heyrovsky}, \tag{12}$$

$$2MH_{ads} \to H_2 + 2M\ \textit{Tafel}. \tag{13}$$

The HER kinetics are supposed to be controlled by the charge transfers of metallic cations [2, 40]. The rate *Vi* of each stage *i* can then be expressed according to the rate of surface covering Q by adsorbed hydrogen H_{ads}.

3.2 Electrodeposition of Ni by Chronoamerometry

The current transients shown in Figure 4 provide key information on the nucleation and growth mechanisms occurring during the electrodeposition of Ni, Fe, and Ni-Fe alloys. In the case of monometallic Ni and Fe deposits (Figs. 4a and 4b), the typical transient profile, characterized initially by a decrease in current density over time, reflects the local depletion of metal ions near the electrode, as well as the increase in diffusion resistance due to deposit thickening. This is followed by a rapid increase in current until it reaches a maximum value, denoted i_{max}, corresponding to a maximum time t_{max}, followed by progressive stabilization. This behavior highlights instantaneous nucleation accompanied by diffusion-controlled growth of Ni and Fe metallic species in solution. For the direct electrodeposition of the Ni–Fe alloy (Fig. 4c), the current transients exhibit more complex behavior, resulting from the simultaneous co-reduction of Ni^{2+} and Fe^{2+} ions. This kinetics is strongly influenced by the phenomenon of anomalous iron deposition, leading to a modification of the current density and growth mechanisms compared to monometallic deposition. Competition between metallic species and differences in reduction overpotentials promote heterogeneous nucleation and a less homogeneous microstructure. In contrast, the pulsed deposition of the Ni–Fe alloy (Fig. 4d) is characterized by higher instantaneous current densities during cathode pulses, followed by relaxation periods that allow for the reconstitution of the diffusion layer. This deposition mode promotes an increased density of nucleation sites, limits local depletion of metal ions, and leads to more uniform and finer deposit growth. Thus, pulsed electrodeposition improves the kinetic control of the process and allows for more homogeneous Ni–Fe layers, characterized by a refined microstructure and superior physico-chemical properties compared to direct deposition.

In general, these curves have the same shape. At the beginning, a decrease in the current density is observed, that is due to the double layer charge. Then this density increases until reaching a maximum value indicated by i_{max} corresponding to a maximum time t_{max}. This behavior shows the formation of one well new phase, which corresponds to the nucleation and the growth of Ni and Fe crystals. Finally, a pseudo-stationary mode is established in accordance with the equation of Cottrell [41]:

$$i = n.F.C.(\frac{D}{\pi t})^{1/2} \tag{14}$$

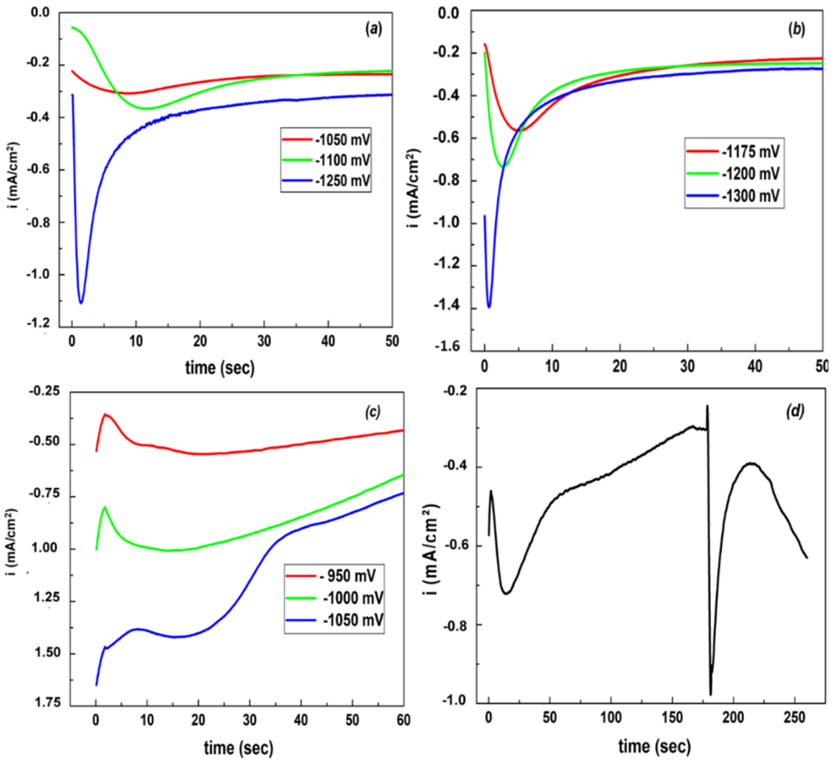

Figure 4. Current transients for the electrodeposition of (a) Ni (b) Fe (c) direct Ni-Fe and (d) pulsed Ni-Fe

3.3. Scharifker–Hills proposed model

Nucleation and the first growth steps are important parameters for understanding the properties of a crystallized deposit, by analyzing the first stages of electrodeposition, using the first part of the chronoamperograms i.e. before the diffusion step limit established. Instantaneous nucleation is defined by a slow growth of nuclei on a low number of active sites, all activated at the same time. However, progressive nucleation corresponds to a rapid growth of nuclei on numerous active sites, all activated during the course of electroreduction [42]. In this case, from Scharifker–Hills model [43], we distinguish the instantaneous nucleation followed by three-dimensional diffusion-limited growth (15) and progressive nucleation followed by three-dimensional diffusion-limited growth (16):

$$\frac{i^2}{i^2_{max}} = 1.9542\left(\frac{t_{max}}{t}\right)[1 - \exp\left(-1.2564\frac{t}{t_{max}}\right)]^2 \tag{15}$$

$$\frac{i^2}{i^2_{max}} = 1.2254\left(\frac{t_{max}}{t}\right)[1 - \exp\left(-2.3367\frac{t^2}{t^2_{max}}\right)]^2 \tag{16}$$

Fig. 5a and 5b show the deposition transient for Ni and Fe electrodeposited from sulfate electrolytes.

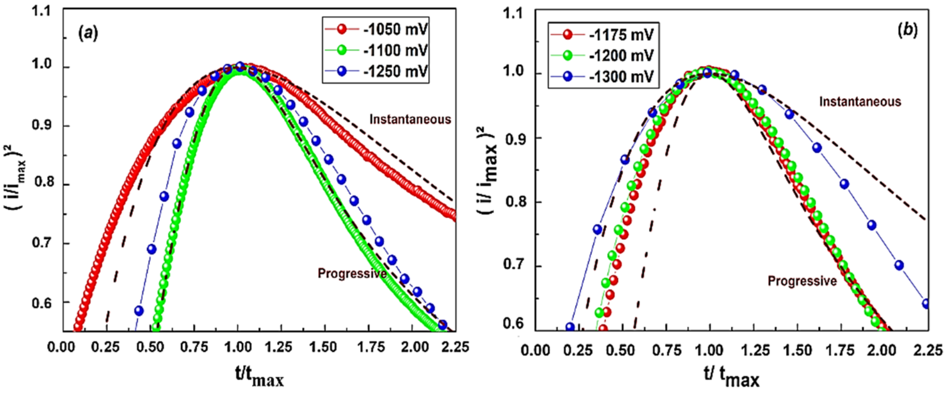

Figure 5. Reduced dimensionless parameters with theoretical curves for progressive and instantaneous nucleation (dotted line) for the deposition of Ni (a) and Fe (b)

The dashed and full lines represent the theoretical curves for progressive and instantaneous limiting cases, described by Eqs. (15) and (16). According to Fig. 5a, the reduced forms for Ni electrodeposition follow the progressive nucleation model for -1100 and -1250 mV/ SCE and an instantaneous nucleation model for -1050 mV/ SCE as obtained by *Azizi et al*., [44]. On the other hand, in Fig. 5b, the Fe electrodeposition at -1300 mV/SCE followed the instantaneous nucleation and a transition from the instantaneous to the progressive nucleation mode. These behaviors are consistent with nucleation of 3D clusters followed by diffusion-limited growth.

3.4 X-ray diffraction characterization

XRD patterns of Fe, Ni, pull Ni-Fe and Ni-Fe are presented in Fig. 7. The data recording was carried out within an angle range from 20° to 80° with a step of 0.02°. The peaks at 44,70 ° and 52,02° are indexed to the diffractions of (111), (200) planes of Ni-Fe structure. The peaks found at $2\theta = 44.06^\circ$ and $2\theta = 43.85^\circ$ are assigned to the preferential diffraction peaks of (111) planes of pulsed and direct Ni-Fe films respectively [45].

The analysis of the structural properties of Ni, Fe and Ni-Fe layers obtained by electrodeposition was carried out by using XRD and the results are presented in Fig. 7. An angular range between 20° and 80° was swept using a step of 0.02°. The two peaks of Ni-Fe diffraction observed are located at the angles of 44,70 ° and 52,02° and were identified as < 111 > and < 200 > of the Ni-Fe alloy respectively. The located peaks of $2\theta = 44.06^\circ$ and $2\theta = 43.85^\circ$ for pulsed and direct Ni-Fe films respectively, have been assigned to be the preferential <111> Ni-Fe face centered cubic (FCC) phase as found by A. Guittoum et al. [45]. All XRD parameters are summarized in Table 2.

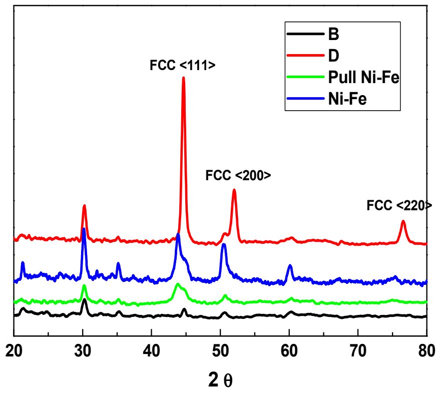

Figure 6. XRD patterns of different deposits.

Table 2. XRD Parameters

Sample	2θ (°)	a(Å)	d(Å)	D (nm)
Ni	44.56	3.51	2.03	26.62
Fe	44.81	3.49	2.02	30.37
Pulsed Ni-Fe	44.06	3.55	2.05	9.77
Ni-Fe	43.85	3.57	2.06	14.63

The evolution of lattice parameter (Å) is represented in the DRX table. We notice a variation in a parameter when we switch the mode from pulse to direct electrodeposition, from 3.55 Å to 3.57 Å. It is to notice that all parameter values of (a) for Ni-Fe alloys obtained by direct and pulsed electrodeposition are superior to that of massive Ni-Fe (a= 3.53 Å) [46], this difference between the experimental values of the a parameter and the value of the solid mass's one is probably due to the residual stresses [47].

The crystallite size of the electrodeposited Ni, Fe and Ni-Fe films were determined from widths (FWHM) of X-ray diffraction peaks using Scherer's formula [48]:

$$D = \frac{0.9\lambda}{\beta Sin\theta} \tag{17}$$

Where λ is the wavelength of the Cu$K\alpha$ radiation, θ is the diffraction angle of reflection and β is the FWHM (full width at half maximum) of the diffraction line.

The crystallite size increases from 9.77 nm to 14.63 nm in pulsed- and direct-electrodeposited Ni-Fe. This behavior can be attributed to the fact that the grains tend to agglomerate with the change from pulsed to direct applied potentials. It is worth mentioning that Chen et al. [49] have found the same crystallite size of 9 nm for $Ni_{80}Fe_{20}$ Permalloy films. Sam et al. [50] reported a crystallite size of 16 nm, so the electrodeposited Ni-Fe crystallite sizes presented in this work are in the average reported in the literature.

3.5. Atomic force microscopy (AFM) characterization

In order to better measure the roughness of these samples, we based on the measurement of the factor of roughness RMS to the surface of the software WSxM software [51]. AFM analysis was carried out to observe the surface morphology of direct and pulse electrodeposited Ni-Fe films. Fig. 8 shows the topographies of the electrodeposits, the results of the analysis indicate the presence of islands with different shape, size and number. This is well described according to the

"Volmer-Weber" mode i.e. the binding energy between metal ad-atom and substrate atoms is smaller than the binding energy between metal ad-atoms themselves, which leads over potential deposition (OPD) of a 3D metal forming on substrate. For the pulse electrodeposited Ni-Fe alloys, Fig. 8 shows a large number of islands covering irregularly the surface of the films, explaining the rough surface and the RMS (Root-Mean-Square) value of 55.78 nm. However, for the direct electrodposition, it was clearly observed a diminution in the number and the size of Ni-Fe islands smoothly dispersed on the surface, leading to low roughness than the pulsed method. The RMS was found to be 7.27 nm for the direct electrodeposition of Ni-Fe as it is summarized in the table 3. Moreover, some holes, that are due to the hydrogen bubbles release on the surface of the deposits, are observed; thereby inhibiting the deposition rate of the alloy in some surface sites that which lead to the appearance of holes observed on images.

By way of comparison, Neagu et al. [52] have obtained a roughness lower than 25 nm for Ni-Fe films prepared by pulsated laser deposition using a substrate of glass. Amrani et al [53] found rms values of 11.5, 14.7 and 0.27 nm.

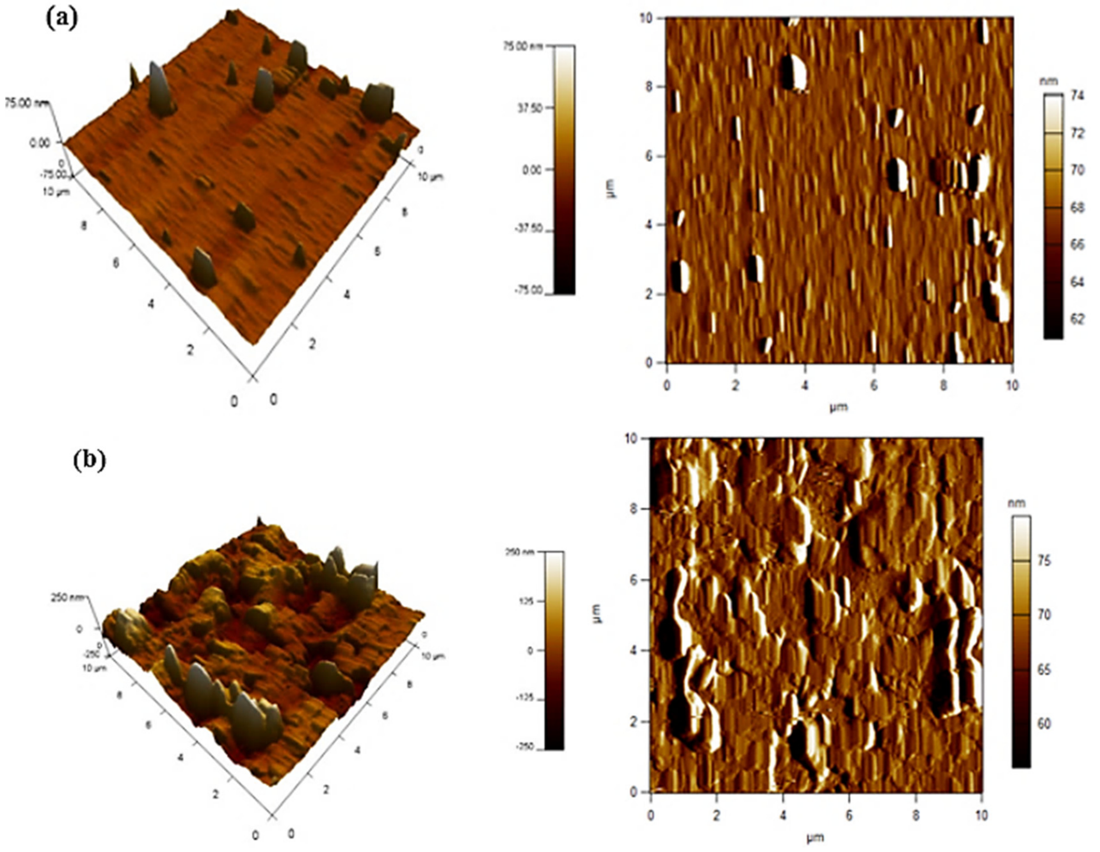

Figure 7. AFM micrographs of: (a) direct Ni-Fe, (b) pulsed Ni-Fe deposits

Table. 3 Root mean square roughness (RMS), crystallite size (D), and interplanar spacing (d) for direct and pulsed Ni–Fe deposits.

Sample	RMS (nm)	d(Å)	D (nm)
Direct Ni-Fe	7.27	2.06	14.63
Pulsed Ni-Fe	55.78	2.05	9.77

4. CONCLUSIONS

In this work, we investigated the influence of direct and pulsed electrodeposition modes on the electrochemical, structural, and morphological properties of Ni-Fe nanostructures electrodeposited on ITO substrates. The deposits were characterized at different stages of fabrication using complementary techniques, namely X-ray diffraction (XRD) and atomic force microscopy (AFM). The electrochemical results identified an optimal potential range between −0.9 and −1.2 V, favorable to the simultaneous reduction of Ni^{2+} and Fe^{2+} ions and the homogeneous formation of the Ni-Fe alloy. Analysis of current transients, interpreted using the Scharifker–Hills theoretical model, reveals a strong dependence of the nucleation and growth mechanisms on the applied potential. In particular, the increased overpotential induces more intense nucleation, reflecting an increase in the density of active nuclei and a significant modification of the deposit growth kinetics. XRD structural analyses reveal the formation of a face-centered cubic (FCC) phase characteristic of the Ni-Fe system, with a marked preferential orientation along the ⟨111⟩ plane. A significant variation in crystallite size is observed depending on the electrodeposition mode. Deposits obtained in pulsed mode exhibit smaller crystallites (≈ 9.77 nm) compared to those produced in continuous mode (≈ 14.63 nm). This reduction is attributed to the alternating current pulses, which limit excessive nuclear growth and promote the formation of finer, more controlled nanostructures.

Such crystalline refinement represents a major advantage for electronic and magnetic applications, where microstructure plays a crucial role in functional performance. AFM morphological analysis shows that the electrodeposition mode directly influences the topography and surface roughness of the films. Layers deposited in pulsed mode exhibit a relatively high roughness (≈ 55.78 nm), reflecting heterogeneous growth associated with a high density of nucleation sites. Conversely, films obtained by direct electrodeposition exhibit a more homogeneous, smoother surface, with an average roughness of approximately 7.27 nm. AFM images indicate three-dimensional Volmer-Weber-type growth, characterized by the formation of islands whose number and size vary with the applied electrochemical conditions. Overall, these results highlight the key role of the electrodeposition mode in controlling the structure, morphology, and properties of Ni-Fe nanostructures. They open up interesting prospects for optimizing these materials for advanced technological applications. However, the complexity of the phenomena involved in the electrodeposition of Ni-Fe alloys on ITO substrates suggests that further investigations, particularly into functional magnetic and electrochemical properties, will be necessary to deepen our understanding of the underlying mechanisms.

Acknowledgment

The authors would like to acknowledge Dr. Yazid Messoudi (LCIMN, UFAS-1), Ms. Djedjiga Haouanoh (URMPE, UMBB) and Pr. Mohamed Hamidouche (URME, UFAS-1) for providing AFM-DRX analysis.

ORCID

Houssem Eddine El Yamine Sakhraoui, https://orcid.org/0000-0002-8563-2087
Djamel Eddine Belfennache, https://orcid.org/0000-0002-4908-6058
Radhia Yekhlef, https://orcid.org/0000-0003-0646-6453
Mohamed A. Ali, https://orcid.org/0000-0002-7390-8592
Hamad M Adress Hasan, https://orcid.org/0000-0002-6739-8311
Hanan F. Emrayed, https://orcid.org/0009-0008-6812-4268
Ghada M Salem, https://orcid.org/0000-0002-1830-7049

REFERENCES

[1] J.W. Gooch, *Lead-Based Paint Handbook*, (Kluwer, New York, 2006), pp. 13–33.
[2] A.S.H. Makhlouf, I. Tiginyanu, (Eds.), *Nanocoatings and ultra-thin films: Technologies and applications*, (Elsevier, 2011).
[3] Q. Zhau, M.H. Chua, P.J. Ong, J.J.C. Lee, K.L.O. Chin, S. Wang, D. Kai, *et al.*, Mater. Today Adv. **15**, 100270 (2022). https://doi.org/10.1016/j.mtadv.2022.100270
[4] A. S. Samra, S. Zafar, M. Ahmad, M. Husnain, R. Kahraman, B. Mansoor, K. Ali, and R.A. Shakoor, Mater. Sci. Eng. B, **327**, 119222 (2026). https://doi.org/10.1016/j.mseb.2026.119222
[5] H. Xing, Z. Shi, S. Yang, and R. Zhang, J. Indian Chem. Soc., **103**(3), 102458 (2026), https://doi.org/10.1016/j.jics.2026.102458
[6] Y. Achour, Y. Benkrima, I. Lefkaier, and D. Belfennache, J. Nano- Electron. Phys. **15**(1), 01018 (2023). https://doi.org/10.21272/jnep.15(1).01018
[7] Y. Benkrima, A.M. Ghaleb, D. Belfennache, R. Yekhlef, and A. Benameur, Funct. Mater. **30 (3)**, 350 (2023). https://doi.org/10.15407/fm30.03.350
[8] G. Wang, Z. Liu, J. Niu, W. Huang, and B. Wang, J. Mater. Res. Technol. **9**, 253 (2020). https://doi.org/10.1016/j.jmrt.2019.10.053
[9] P.K. Rai, and A. Gupta, Mater Today Proc. **44**, 1079 (2021). https://doi.org/10.1016/j.matpr.2020.11.182
[10] S. Mahdid, D. Belfennache, D. Madi, M. Samah, R. Yekhlef, and Y. Benkrima, J. Ovonic. Res. **19(5)**, 535-545 (2023). https://doi.org/10.15251/JOR.2023.195.535
[11] Y. Li, Z. Yang, H. Han, M. Liu, M. Zhang, Z. Wang, and T. Wu, J. Mater. Res. Technol. **15**. 924 (2021). https://doi.org/10.1016/j.jmrt.2021.08.077
[12] M.H. Sliem, K. Shahzad, V.N. Sivaprasad, R.A. Shakoor, A.M. Abdullah, O. Fayyaz, R. Kahraman, and M.A. Umer, Surf. Coatings Technol. **403**, 126340 (2020). https://doi.org/10.1016/j.surfcoat.2020.126340
[13] L. Huang, Q. Dai, W. Huang, and X. Wang, Appl. Surf. Sci. **572**, 51534 (2022). https://doi.org/10.1016/j.apsusc.2021.151534
[14] J. Guo, P. Qin, Z. Ma, Q-L. Yang, J. Feng, Z-H. Ge, Scr. Mater. **164**, 71 (2019). https://doi.org/10.1016/j.scriptamat.2019.01.039
[15] C. Dong, R. Wang, and S. Guo, Coatings, **9**, 1854 (2019). https://doi.org/10.3390/coatings9120820
[16] C. Liu, F. Su, and J. Liang, Trans. Nonferrous Met. Soc. China, **28**, 2489 (2018). https://doi.org/10.1016/S1003-6326(18)64895-2
[17] A. Gupta, and C. Srivastava, Philos. Mag. **101**, 2036 (2021). https://doi.org/10.1080/14786435.2021.1949067
[18] V. Torabinejad, M. Aliofkhazraei, A.S. Rouhaghdam, and M.H. Allahyarzadeh, Mater. Corros. **68**, 347 (2017). https://doi.org/10.1002/maco.201609071
[19] M.R.Z. Meymian, A. Ghaffarinejad, R. Fazli, and A.K. Mehr, Colloids Surfaces A Physicochem. Eng. Asp. **593**, 124617 (2020). https://doi.org/10.1016/j.colsurfa.2020.124617
[20] X. Hu, and N. Qu, Thin Solid Films, **700**, 137923 (2020). https://doi.org/10.1016/j.tsf.2020.137923
[21] F. Saker, L. Remache, D. Belfennache, K.R. Chebouki, and R. Yekhlef, Chalcogenide Lett. **22**(2), 151 (2025). https://doi.org/10.15251/CL.2025.222.151
[22] Y. Bellal, A. Bouhank, D. Belfennache, and R. Yekhlef, East Eur. J. Phys. (1), 170 (2025). https://doi.org/10.26565/2312-4334-2025-1-16
[23] F. Hadji, Y. Rassim, D. Belfennache, R. Yekhlef, N. Bounar, M.A. Bradai, M. Hemdan, and M.A. Ali, Egypt. J. Chem. **68**, 63 (2025). https://doi.org/10.21608/ejchem.2024.283147.9600
[24] R. Ouldamer, D. Madi, and D. Belfennache, in: *Advanced Computational Techniques for Renewable Energy Systems, IC-AIRES, 2022, Lecture Notes in Networks and Systems*, 591, edited by M. Hatti, (Springer, Cham. 2023). pp. 700-705. https://doi.org/10.1007/978-3-031-21216-1_71

[25] I. Gurrappa, and L. Binder, Sci. Technol. Adv. Mater. **9**(4), (2008) https://doi.org/10.1088/1468-6996/9/4/043001
[26] H. Li, X. Zhao, S. Cao, K. Li, M. Chen, Z. Xu, J. Lu, and L. Zhang, Appl. Surf. Sci. **263**, 163 (2012). https://doi.org/10.1016/j.apsusc.2012.09.022
[27] A.R. Boccaccini, S. Keim, R. Ma, Y. Li, and I. Zhitomirsky, J. R. Soc. Interface. **7**, S581 (2010). https://doi.org/10.1098/rsif.2010.0156.focus
[28] A. Chavez-Valdez, M.S.P. Shaffer, and A.R. Boccaccini, J. Phys. Chem. B, **117**, 1502 (2013). https://doi.org/10.1021/jp3064917
[29] L. Hasniou, B. Nessark, and N. Maouche, Russ. J. Appl. Chem. **90**, 633 (2017). https://doi.org/10.1134/S1070427217040206
[30] N. Maouche, M. Guergouri, S. Gam-Derouich, M. Jouini, B. Nessark, and M.M. Chehimi, J. Electroanal. Chem, **685**, 21 (2012). https://doi.org/10.1016/j.jelechem.2012.08.020
[31] Z. Ait-Touchente, H.E. el-Jamine Sakhraoui, N. Fourati, C. Zerrouki, N. Maouche, R. Touzani, N. Yaakoubi, *et al*., Proceedings. MDPI, **2**(13), 1004 (2018). https://doi.org/10.3390/proceedings2131004
[32] O. Dilmi, and M. Benaicha, Russ. J. Electrochem. **53**, 140 (2017). https://doi.org/10.1134/S1023193517020045
[33] B. Scharifker, and G. Hills, Electrochim. Acta. **28**, 879 (1983). https://doi.org/10.1016/0013-4686(83)85163-9
[34] D. Pletcher, R. Greff, R. Peat, L.M. Peter, and J. Robinson, Instrumental methods in electrochemistry, 317-355 (2010). https://doi.org/10.1533/9781782420545.317
[35] A. Saraby-Reintjes, and M. Fleischmann, Electrochim. Acta. **29**, 557 (1984). https://doi.org/10.1016/0013-4686(84)87109-1
[36] S.L. Díaz, J.A. Calderón, O.E. Barcia, and O.R. Mattos, Electrochim. Acta. **53**, 7426 (2008). https://doi.org/10.1016/j.electacta.2008.01.015
[37] H. Dahms, and I.M. Croll, J. Electrochem. Soc. **112**, 771 (1965). https://doi.org/10.1149/1.2423692
[38] L. Giuliani, and M. Lazzari, Electrochim. Met. **3**, 45 (1968).
[39] D. Gangasingh, and J.B. Talbot, J. Electrochem. Soc. **138**, 3605 (1991). https://doi.org/10.1149/1.2085466
[40] Y. Tsuru, M. Nomura, and F.R. Foulkes. J. Appl. Electrochem. **32**, 629 (2002). https://doi.org/10.1023/A:1020130205866
[41] H. He, H. Liu, F. Liu, and K. Zhou, Surf. Coatings Technol. **201**, 958 (2006). https://doi.org/10.1016/j.surfcoat.2006.01.016
[42] F.G. Cottrell, Zeitschrift für Phys Chemie, **42U**, 385 (1903). https://doi.org/10.1515/zpch-1903-4229
[43] M. Palomar-Pardavé, M.T. Ramírez, I. González, A. Serruya, and B.R. Scharifker, J. Electrochem. Soc. **143**, 1551 (1996). https://doi.org/10.1149/1.1836678
[44] A. Azizi, A. Sahari, G. Schmerber, and A. Dinia, Int. J. Nanosci. **7**, 345 (2008). https://doi.org/10.1142/S0219581X08005535
[45] S. Lamrani, A. Guittoum, R. Schäfer, S. Pofahl, V. Neu, M. Hemmous, and N. Benbrahim, EPJ Appl. Phys. **74**, 30302 (2016). https://doi.org/10.1051/epjap/2016150548
[46] T. Yeh, J.M. Sivertsen, and J.H. Judy, IEEE Trans. Magn. **23**, 2215 (1987). https://doi.org/10.1109/TMAG.1987.1065272
[47] S. Kotapati, A. Javed, N. Reeves-Mclaren, M.R.J. Gibbs, and N.A. Morley, J. Magn. Magn. Mater. **331**, 67 (2013). https://doi.org/10.1016/j.jmmm.2012.11.022
[48] B.D. Cullity, *Elements of X-Ray Diffraction*, 2nd Edition, (Addison-Wesley Publishing Company Inc., Phillippines, 1978).
[49] Y.T. Chen, and C.W. Wu, Intermetallics, **34**, 89 (2013). https://doi.org/10.1016/j.intermet.2012.11.006
[50] S. Sam, G. Fortas, A. Guittoum, N. Gabouze, and S. Djebbar, Surf. Sci. **601**, 4270 (2007). https://doi.org/10.1016/j.susc.2007.04.107
[51] I. Horcas, R. Fernández, J.M. Gómez-Rodríguez, J. Colchero, J. Gómez-Herrero, A.M. Baro, Rev. Sci. Instrum. **78**(1), 013705 (2007). https://doi.org/10.1063/1.2432410
[52] M. Neagu, M. Lozovan, M. Dobromir, L. Velicu, C. Hison, and S. Stratulat, J. Optoelectron. Adv. Mater. **10**, 978 (2008).
[53] S. Lamrani, A. Guittoum, R. Schäfer, M. Hemmous, V. Neu, S. Pofahl, T. Hadjersi, and N. Benbrahim, J. Magn. Magn. Mater. **396**, 263 (2015). https://doi.org/10.1016/j.jmmm.2015.07.111

ВПЛИВ РЕЖИМУ ПРЯМОГО ТА ІМПУЛЬСНОГО ЕЛЕКТРООСАДЖЕННЯ НА ЕЛЕКТРОХІМІЧНІ, СТРУКТУРНІ ТА МОРФОЛОГІЧНІ ВЛАСТИВОСТІ ПОКРИТТІВ З НАНОСТРУКТУР Ni-Fe

Хусем Еддін Ель Ямін Сахрауї[1,2], Х. Аяді[3], Н. Мауш[2], Д. Бельфеннаше[4], Р. Єхлеф[4], Мохамед А. Алі[5],
Хамад М. Адресс Хасан[6], Ханан Ф. Емраєд[6], Ханібал Саїд Хатаб[7], Гада М. Салем[8]
[1]Кафедра технологічних процесів, технологічний факультет, Університет Ферхата Аббаса,
Сетіф-1, Сетіф, 19000, Алжир
[2]Лабораторія електрохімії та матеріалів (LEM), Університет Ферхата Аббаса, Сетіф-1, Сетіф, 19000, Алжир
[3]Університет Скікди від 20 серпня 1955 року, Скікда, Алжир
[4]Дослідницький центр промислових технологій (CRTI), поштова скринька 64, Черага, 16014, Алжир, Алжир
[5]Школа біотехнології, Каїрський університет Бадра (BUC), місто Бадр 11829, Каїр, Єгипет
[6]Хімічний факультет, факультет природничих наук, Університет Омара аль-Мухтара, Лівія
[7]Факультет освіти, Аль-Мардж, університет Бенгазі, Лівія
[8]Лівійське управління наукових досліджень, Триполі, Лівія

Наноструктуровані сплави нікель-заліза (Ni-Fe) викликають зростаючий інтерес завдяки своїм чудовим електрохімічним, магнітним та механічним властивостям, що робить їх особливо привабливими для застосування в електрокаталізі, накопиченні енергії, сенсорах та функціональних покриттях. Це дослідження представляє порівняльний аналіз електрохімічних, структурних та морфологічних характеристик наноструктур нікель-заліза (Ni-Fe), синтезованих у сульфатних електролітах на підкладках з оксиду індію-олова (ITO) за допомогою різних методів електроосадження. Виготовлені наноструктури були охарактеризовані за допомогою циклічної вольтамперометрії, хроноамперометричних вимірювань (потенціостатичні кроки), атомно-силової мікроскопії (АСМ) та рентгенівської дифракції (XRD). Процес електрокристалізації був оцінений за допомогою моделі Шаріфкера-Хіллса, яка показала, що механізми зародження відрізняються залежно від застосованих потенціалів. Рентгенівський дифракційний аналіз підтвердив полікристалічну природу наноструктур Ni-Fe з переважною кристалографічною орієнтацією <111> та гранецентрованою кубічною (ГЦК) структурою, що спостерігається в обох режимах осадження. Розміри кристалітів були визначені як 9,77 нм за імпульсних умов та 14,63 нм для прямого методу. Аналіз поверхні за допомогою АСМ додатково показав, що вибір методу електроосадження суттєво впливає на морфологічні особливості отриманих осадів.

Ключові слова: *наноструктури Ni-Fe; метод електроосадження; покриття; підкладка ITO*